PCCP

Accepted Manuscript

ROYAL SOCIETY OF CHEMISTRY

www.rsc.org/pccp

Physical Chemistry Chemical Physics
CREATED USING THE RSC LaTeX PCCP ARTICLE TEMPLATE – SEE www.rsc.org/electronicfiles FOR DETAILS
ARTICLE TYPE www. rsc.org/xxxxxx | XXXXXXXX

EPR-correlated dipolar spectroscopy by Q-band chirp SIFTER†

Andrin Doll,*[a] and Gunnar Jeschke[a]

Received Xth XXXXXXXXXX 20XX, Accepted Xth XXXXXXXXX 20XX
First published on the web Xth XXXXXXXXXX 200X
DOI: 10.1039/b000000x

While two-dimensional correlation spectra contain more information as compared to one-dimensional spectra, typical spectral widths encountered in electron paramagnetic resonance (EPR) spectroscopy largely restrict the applicability of correlation techniques. In essence, the monochromatic excitation pulses established in pulsed EPR often cannot uniformly excite the entire spectrum. Here, this restriction is alleviated for nitroxide spin labels at Q-band microwave frequencies around 35 GHz. This is achieved by substitution of monochromatic pulses by frequency-swept chirp pulses tailored for uniform excitation. Unwanted interference effects brought by this substitution are analyzed for a pair of electron spins with secular dipolar coupling. Experimentally, the dipole-dipole interaction can be separated from other interactions by a constant-time Zeeman-compensated solid echo sequence called SIFTER. Such SIFTER experiments usually yield a one-dimensional dipolar spectrum. EPR-correlated dipolar spectra can be obtained when the four pulses are replaced by chirp pulses. These two-dimensional spectra encode additional information on the geometrical arrangement of the two spin labels. With the excitation parameters achieved by a home-built Q-band spectrometer capable of frequency-swept excitation, unwanted interference effects can be largely neglected for the examined model compound with a spin-spin distance of 4 nm. The experimentally obtained correlation pattern conforms to the expectation based on the inter-spin geometry of the investigated rigid model compound.

1 Introduction

Determination of distances in the nanometer range between two electron spins is an important branch of pulsed electron paramagnetic resonance (EPR) spectroscopy. In particular, pairwise distance information gained from spin-labeled biomacromolecules or systems containing paramagnetic cofactors provides valuable insight into molecular structure and function, even if the studied ensemble of molecules is embedded in a disordered solid[1–4]. The pulse sequences used in this context separate the dipolar electron-electron interaction from other interactions. The term pulsed dipolar spectroscopy (PDS) is often used to summarize all relevant pulse sequences. To date, the four-pulse double electron-electron resonance (DEER, also PELDOR) sequence[5] is employed routinely for that purpose. Other approaches, such as the six-pulse double-quantum coherence (DQC) pulse sequence[6], or the four-pulse single frequency technique for refocusing (SIFTER)[7], are applied less frequently. One reason for that is the broad excitation bandwidth required for DQC and SIFTER as compared to DEER. In fact, DEER intrinsically relies on selective pulses, which excite only one of the two coupled spins. DQC and SIFTER on the contrary rely on non-selective pulses, which are pulses that excite both coupled spin partners simultaneously - a requirement that is often difficult to achieve for a sufficiently large fraction of all spin pairs in pulsed EPR with monochromatic excitation pulses.

While all PDS pulse sequences establish controlled evolution of the spins under the dipolar coupling, the underlying spin dynamics are entirely different when using either selective or non-selective pulses. The conceptual difference between the two excitation types can be exemplified with a two-pulse Hahn echo experiment performed on a two-spin system with weak (secular) dipolar coupling[8]: If the two pulses for echo formation selectively excite one of the two coupled spins, the evolution under the secular dipolar interaction is refocused by the selective π pulse. If the two pulses excite both coupled spins simultaneously, the non-selective π pulse fails to refocus the evolution under the dipolar interaction. A Hahn echo formed by non-selective pulses therefore features dipolar modulations as a function of the inter-pulse delay, as demonstrated during the early onset of pulsed EPR[9].

These refocusing properties of non-selective and selective π pulses constitute the principles of the various PDS pulse sequences: The DEER observer sequence employs selective π pulses that refocus the dipolar evolution. Accordingly, time-variable evolution under the dipolar coupling requires a dephasing mechanism, which is provided by the pump pulse that selectively inverts the partner spin. For DQC and SIFTER, the non-selective π pulses do not refocus the dipolar evolution,

† Electronic Supplementary Information (ESI) available: Q-band AWG spectrometer, Dipolar evolution for chirp SIFTER, Supplementary experimental data. See DOI: 10.1039/b000000x/

[a] *Laboratory of Physical Chemistry, ETH Zurich, Vladimir-Prelog-Weg 2, 8093 Zurich, Switzerland. Fax: +41 44 633 1448; Tel: +41 44 632 2735; E-mail: adoll@ethz.ch*

which inhibits deadtime-free PDS experiments. To establish time-variable evolution under the dipolar coupling, a refocusing mechanism needs to be introduced. For DQC, refocusing of the dipolar evolution is achieved by forward/backward transfer to double-quantum coherence. For SIFTER, the dipolar evolution is refocused by a $\pi/2$ pulse applied in quadrature to the excitation pulses, which is the principle of a solid echo sequence[10].

From an experimental viewpoint, a purely selective or a purely non-selective excitation pulse is difficult to implement. In DEER, for instance, there is often overlap between the EPR spectra of the two coupled spin partners, especially if the same type of spin label is used. In addition, the excitation bands of the pump and observer spins often also entail considerable spectral overlap. Accordingly, some spin partners within the studied ensemble are excited non-selectively by either pump or observation pulses. The resulting multitude of residual dipolar evolution pathways has been analyzed recently[11].

For non-selective excitation pulses, as used in DQC and SIFTER, the width of the coupled spins' EPR spectra often exceeds the excitation bandwidth attainable with monochromatic pulses. These experiments therefore often perform non-ideally due to spectrally non-uniform excitation pulses. With monochromatic excitation pulses, best performance has been achieved using intense π pulses with durations as short as 4 ns at microwave frequencies up to 18 GHz[4].

Recently, technological advances allowed to incorporate shaped microwave pulses with enhanced excitation bandwidth into pulsed EPR spectroscopy, as exemplified with optimal control pulses[12] and frequency-swept passage pulses[13,14] at X-band microwave frequencies (9 GHz). Such schemes utilize arbitrary waveform generators, previously applied in continuous-wave EPR experiments[15], EPR imaging[16] and quantum computation[17,18], and can thus exceed excitation bandwidths that were accessible with monochromatic excitation by composite pulses[19]. To date, the majority of experiments for EPR spectroscopy purposes were performed using frequency-swept passage pulses at frequencies up to Q band (35 GHz). Owing to the swept frequency during the pulse, we refer to these pulses as chirp pulses throughout this work. The broad bandwidth achievable with this class of pulses made it a widely used building block in NMR spectroscopy[20]. The passage of the excitation field through resonance can be described analytically using Landau-Zener-Stückelberg-Majorana (LZSM) theory[21,22]. Accordingly, the nominal flip angle can be predicted[23]. Throughout this work, this nominal flip angle is referred to as β_{LZSM}. Note that for $\beta_{\mathrm{LZSM}} \to 180°$, the chirp pulse realizes an adiabatic passage. For β_{LZSM} significantly below 180°, it is more appropriate to refer to a non-adiabatic passage. Note that, in the end, β_{LZSM} is just a more experimentally oriented way of referring to the adiabaticity factor Q_{crit}[24] of a passage pulse.

In EPR spectroscopy, such pulses have been used to improve DEER experiments[13,14,25], including extensions to population transfer in high-spin systems[26] and extensions to multi-pulse DEER[27] to realize PDS with dynamical decoupling[28]. For PDS with non-selective pulses, chirp pulses were shown to yield substantial improvement in data quality of SIFTER experiments[29]. In particular, a large dipolar modulation depth on the order of 95% has been achieved for X-band SIFTER, which confirms non-selective broadband excitation for the majority of coupled spin pairs. At Q band, limitations in power and bandwidth constrained the dipolar modulation depth to 10%.

Moreover, multi-dimensional correlation spectroscopy over broad bandwidths beyond 100 MHz became feasible using chirp pulses. While initial experiments correlated longitudinal relaxation and nuclear modulation to the FT EPR spectrum[30], the methodology has been extended to obtain two- and three-dimensional spectra which correlate the FT EPR spectrum to electron spin echo envelope modulation (ESEEM) frequencies due to coupled nuclei[31].

An important distinction between chirp pulses and monochromatic pulses arises from the spin dynamics during the pulse. While a chirp pulse passes through the EPR spectrum, different transitions are excited at different times. This can cause unwanted frequency dispersion and interference, which may lead to different results as compared to experiments performed with monochromatic pulses that excite all transitions simultaneously[23,32,33]. As an example, a two-pulse echo with chirp pulses requires a $\pi/2$ pulse that has twice the duration of the π pulse to refocus the resonance offset without frequency dispersion[34,35]. Another relevant example is four-pulse DEER with a chirp pump pulse, where the pump pulse duration needs to be short compared to dipolar evolution periods to keep the frequency dispersion negligible[13]. This limitation may be circumvented by refocusing the frequency-dispersed dipolar evolution using an even number of pump pulses in multi-pulse DEER[14]. An effect related to chirp excitation has also been observed in three-pulse EPR-correlated ESEEM experiments[31], where the resulting correlation spectra no longer had the symmetry that one would expect for monochromatic excitation pulses[36].

In the present work, we extend our methodology of FT EPR correlation spectroscopy with chirp pulses to Q-band frequencies and to systems with dipolar coupling. In particular, we aim for EPR-correlated PDS with nitroxides using the SIFTER pulse sequence. As compared to the established one-dimensional techniques, EPR-correlated dipolar spectra are advantageous to identify relative spin orientations, as studied theoretically within the context of EPR-correlated DQC experiments[37]. Experimentally, however, it has not yet been feasible to correlate the dipolar frequencies to the entire FT EPR spectrum due to the overall experimental bandwidth lim-

ited to roughly 100 MHz[4,38].
This paper is organized as follows. First, the experimental methods and calculations performed within this study are outlined in Section 2. Then, results and discussion follow, where the performance of Q-band FT EPR with nitroxides is presented in Section 3.1. This capability is applied to a pair of nitroxides in Section 3.2, where chirp effects in the dipolar evolution of a two-pulse chirp echo are studied. A SIFTER pulse sequence for FT EPR purposes is introduced and analyzed in Section 3.3, which includes experimental data that shows pronounced correlations between the EPR and the dipolar spectrum.

2 Materials and Methods

2.1 Instrumentation

The UWB spectrometer used in this work is a high-power Q-band extension of our home-built X-band UWB spectrometer[30]. The basic topology of the spectrometer at Q band is analogous to the X-band implementation. In particular, the *input* to this spectrometer is a digital realization of the pulse sequence to be synthesized by an 8 GSa/s arbitrary waveform generator (AWG). The oscillation frequencies of the pulses output by the AWG lie within a $1-2$ GHz frequency range. By mixing with a frequency-adjustable reference oscillator around 33 GHz, the pulse sequence is up-converted to the desired Q-band frequency window. During detection, the same reference oscillator is used for down-conversion of spin echoes at Q band back to the $1-2$ GHz frequency window. The *outputs* of the spectrometer are digitized and averaged transients of the relevant spin echo, which are evaluated further digitally[30].
The Q-band microwave transceiver has a similar layout as the X-band microwave transceiver. A detailed description of the Q-band transceiver is provided in the ESI. For efficient use of the nominal 200 W output power of the microwave amplifier over a broad bandwidth, a home-built loop-gap resonator with quality factor $Q_\mathrm{L} = 120$ accepting 1.6 mm outer-diameter sample tubes was employed.

2.2 Pulse sequences

All experiments were performed at 50 K at a repetition rate of 3 ms. All chirp pulses swept their frequency over a range of $\Delta f = 500$ MHz and compensated for the experimental resonator profile $\nu_1(f)$ by adaptation of the frequency modulation function[13]. The pulses had durations of either 128 or 64 ns. Independent on the pulse duration, the leading and trailing flanks of the pulse were smoothened during 30 ns by a quarter period of a sine[33].
The SIFTER pulse sequence is formally parameterized by $(\pi/2)_x - \tau_1 - (\pi)_x - \tau_1 - (\pi/2)_y - \tau_2 - (\pi)_x - \tau_2 -$ echo and is illustrated further below in Fig. 3. The pulse delays τ_1 and τ_2 were varied with a step size of 12 ns, which resulted in a 24 ns time increment of the dipolar evolution time t. In total, the time t was stepped from -19.704 μs to 19.704 μs using 1643 points. The echo position $2(\tau_1+\tau_2)$ was varied to characterize and average residual modulations, starting from 40 μs using an increment of 392 ns for 12 datasets (see also ESI). The acquisition of one dataset required 2.3 hours and already led to a very large signal-to-noise ratio (SNR).
The phases of the second, third and fourth pulse were varied according to the reported 16-step phase cycle[7]. The four chirp pulses had durations of 128, 128, 128, and 64 ns, which corresponds to a 2:2:2:1 scheme. The rationale for this choice is given below.
The amplitudes of the four SIFTER pulses were set up by maximizing the echo amplitude while incrementing pulse amplitudes. First, the amplitudes of the two $\pi/2$ pulses were optimized concurrently. Then, the two π pulses were optimized, one after another.

2.3 Product operator calculations

Product operator formalism[39] was used to analyze the frequency dispersion resulting from chirp excitation. The calculations were performed in Mathematica using the SpinOp library[40]. Within the scope of this study, a two-spin system with weak dipolar interaction was considered, hence

$$\hat{\mathscr{H}}_0 = \Omega_1 \hat{S}_{1,\,\mathrm{z}} + \Omega_2 \hat{S}_{2,\,\mathrm{z}} + \omega_\mathrm{dd} \hat{S}_{1,\,\mathrm{z}} \hat{S}_{2,\,\mathrm{z}} \qquad (1)$$

where the resonance offsets Ω_i, in a frame rotating with the inital frequency of the sweep, and the coupling ω_dd have units of angular frequencies.
A monochromatic non-selective pulse with flip angle β followed by a delay τ is calculated as

$$\hat{\sigma}_1 \xrightarrow{\beta(\hat{S}_{1,\,\mathrm{x}}+\hat{S}_{2,\,\mathrm{x}})} \hat{\sigma}_{\mathrm{m},\,2} \xrightarrow{\tau\hat{\mathscr{H}}_0} \hat{\sigma}_{\mathrm{m},\,3} \qquad (2)$$

To incorporate the chirp pulse, a linear frequency sweep with inverse sweep rate $k = t_\mathrm{p}/(2\pi\Delta f)$ was considered. Accordingly, the basic pulse-delay building block in Eq. (2) was replaced by two consecutive pulses with timing determined by $k\Omega_i$, where the first pulse excites spin 1 and the second pulse spin 2:

$$\begin{aligned} &\hat{\sigma}_1 \xrightarrow{k\Omega_1\hat{\mathscr{H}}_0} \hat{\sigma}_2 \xrightarrow{\beta\hat{S}_{1,\,\mathrm{x}}} \hat{\sigma}_3 \xrightarrow{k(\Omega_2-\Omega_1)\hat{\mathscr{H}}_0} \hat{\sigma}_4 \\ &\hat{\sigma}_4 \xrightarrow{\beta\hat{S}_{2,\,\mathrm{x}}} \hat{\sigma}_5 \xrightarrow{(\tau-k\Omega_2)\hat{\mathscr{H}}_0} \hat{\sigma}_6 \end{aligned} \qquad (3)$$

For multi-pulse sequences, such blocks were concatenated and the inverse sweep rate k was scaled according to the relative pulse duration of each chirp pulse. For the 2 : 1 chirp echo

scheme, for instance, we used $2k$ and k for the first and second pulse, respectively. The echo modulation formulas were obtained by computation of the expectation values of $\hat{S}_{1,\,y}$ and $\hat{S}_{2,\,y}$ at the position of the echo maximum. In the absence of the coupling ω_{dd}, all considered sequences produced an unity output, which affirms refocusing of the resonance offset without frequency dispersion. For ease of further analysis, the modulation formulas including the dipolar coupling were rewritten using the delays $\delta_1 = 2k\Omega_1$ and $\delta_{12} = 2k(\Omega_2 - \Omega_1)$. Since the first pulse in all considered sequences had an inverse sweep rate of $2k$, the delay δ_1 is the time offset until the first spin is excited by the first pulse, whereas δ_{12} is the time delay between excitation of the two spins. A schematic representation of these delays is given below in Fig. 2a.

Note that the calculation procedure is analogous to previous considerations in NMR for a two-spin system with weak coupling, where the field strength of the pulse exceeds the coupling strength[41]. This approximation is also justified for our experimental conditions.

2.4 Sample preparation

TEMPOL was purchased from Sigma-Aldrich and used as received. The 1 mM solution used in the experiments in Section 3.1 was prepared from a 100 mM stock solution in milli-Q water, by diluting to 2 mM and mixing with glycerol (1:1 in volume).

As a model biradical with well-defined mutual geometry for EPR-correlated PDS experiments, a nitroxide-ruler holding two nitroxide spin labels at a distance of about 4.0 nm was used. The synthesis and EPR characterization of this ruler have been reported elsewhere[42,43]. The structure of the ruler will be shown further below in Fig. 5d, where the geometry of the ruler will be relevant for interpreting experimental results. For all EPR experiments, the compound has been dissolved to a concentration of 50 μM in a deuterated ortho-terphenyl solvent, which provides very long phase memory times at the measurement temperature of 50 K.

3 Results and discussion

3.1 Q-band FT EPR with nitroxides

In analogy with our previous results at X band[30], the performance of Q-band chirp FT EPR was tested using a TEMPOL reference at 1 mM concentration. In a first step, the improvement in excitation bandwidth when going from monochromatic to chirp excitation is demonstrated. With monochromatic pulses, optimum pulse durations for $\pi/2$ and π pulses were 2.75 ns and 5.5 ns, respectively, at the center of the resonator. Optimization of the chirp pulse amplitudes resulted in pulses with nominal flip angles $\beta_{LZSM} = 116°$ and $\beta_{LZSM} = 160°$.

The resulting FT spectra are shown in Fig. 1a, showing the real (solid) and imaginary (dashed) FT components for the chirp echo (black) and the Hahn echo (gray). While the Hahn echo mainly captures the principal nitroxide peak, the chirp echo FT spectrum resembles the entire nitroxide spectrum. The black up-arrow marks the low-frequency shoulder of the spectrum, where the improvement is most apparent. The down-arrow at the principal nitroxide peak denotes an overall signal loss of the chirp echo spectrum as compared to the Hahn echo spectrum. In analogy to our results at X band, the additional loss in the chirp echo spectrum originates from instantaneous diffusion, which is maximized when exciting the entire nitroxide spectrum[44,45].

For multi-pulse sequences, excitation pulses with spectrally uniform excitation profiles are crucial. In order to affirm that our bandwidth-compensated chirp pulses are also largely uniform at Q band, the FT EPR spectrum was compared to the conventional field-swept spectrum. Due to encoding of nuclear modulations along the frequency axis, several FT EPR spectra at different pulse delays were summed[30]. In fact, we detected nuclear modulations around 106 MHz (see ESI), which is the double proton frequency originating from surrounding matrix protons[46]. The modulation-averaged FT EPR spectrum is shown in black in Fig. 1b and is superimposed

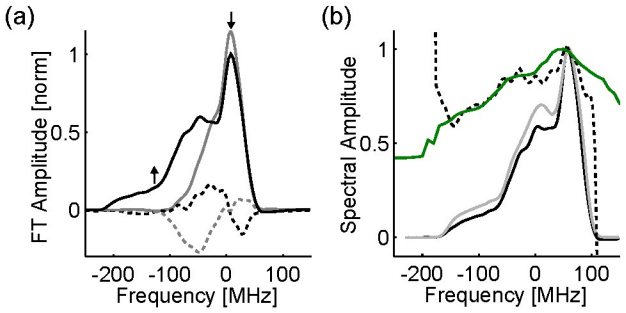

Fig. 1 Q-band FT EPR with nitroxides. (a) Real part (solid lines) and imaginary part (dashed lines) of chirp echo (black) and Hahn echo (gray) in frequency domain. The arrows indicate the performance of the chirp echo relative to the Hahn echo (up-arrow: better performance, down-arrow: worse performance) (b) Real part of chirp echo in frequency domain averaged over several nuclear modulation periods (solid black) and conventional field-swept echo-detected spectrum converted to a frequency scale (gray). The ratio between the two spectra (dashed black) shows the perturbation of the chirp echo spectrum, which appears to be dominated by the resonator that is indicated by $\nu_1(f)$ obtained at full-scale (green). Note that the frequency axes in the two plots have a different zero-point. In panel (a), the zero frequency corresponds to the excitation frequency of the monochromatic pulse. In panel (b), the zero frequency is the central frequency of the chirp pulse.

by the field-swept spectrum cast to a frequency axis (gray). The ratio between these spectra illustrated by the dashed black curve represents the spectral attenuation superimposed on the FT EPR spectrum. When using ideally uniform excitation pulses on $S = 1/2$ spin systems, this attenuation originates solely from the resonator profile (green) during the detection process[30]. The good agreement between the curves affirms that our pulses are largely uniform. Further information is found in the ESI, where experimental excitation profiles of various pulses are compared.

3.2 Chirp effects in dipolar evolution

When applying chirp pulses to systems with dipolar coupling, eventual limitations due to the influence of the frequency-progressive excitation on dipolar evolution are important to identify. To simplify the analysis, these are first shown for a two-pulse chirp echo using nitroxides, before proceeding to the more elaborate case of four-pulse SIFTER presented in Section 3.3.

The timing of the pulse sequence is given in Fig. 2a, where the pulses for coherence excitation (FP90) and refocusing (FP180) are illustrated by their time-frequency profiles. For illustration purposes, linear frequency sweeps are considered. For a two-spin system according to Eq. (1), the first spin S_1 is excited at a time $t = \delta_1$, whereas the second spin S_2 is excited after an additional delay δ_{12}. While this 2:1 chirp echo pulse sequence refocuses the frequency dispersion of the resonance offset at $t = 2\tau$, the situation is different for the dipolar coupling. Application of the product operator formalism results in the modulation formulas (see Section 2.3)

$$\langle \hat{S}_{y,1} \rangle (2\tau) = -\cos(\omega_{dd}(\tau - \delta_1/2 - \delta_{12})) \cdot \cos(\omega_{dd}\delta_{12}/2) \quad (4)$$

$$\langle \hat{S}_{y,2} \rangle (2\tau) = -\cos(\omega_{dd}(\tau - \delta_1/2 - \delta_{12})) \quad (5)$$

As can be seen, the first cosine factor in each equation is identical. However, the modulation amplitude of the first spin is influenced by an additional cosine factor.

The dependence of the first cosine factor on δ_1 and δ_{12} can be understood by considering spin 2, whose evolution initiates at $t = \delta_1 + \delta_{12}$. Starting from this point until echo formation, the maximum phase to be acquired under ω_{dd} is $\phi_{max} = \omega_{dd}(\tau - \delta_1/2 - \delta_{12}/2)$. However, the FP180 pulse refocuses part of this evolution, since the two spins are not inverted simultaneously, but with a gap in between. This reduces ϕ_{max} by $\omega_{dd}\delta_{12}/2$ and explains the phase in the first cosine factor.

The additional cosine factor arises due to the asymmetry of the excitation scheme and has its origin in the first δ_{12} evolution period, where only S_1 evolves. In particular, coherent excitation of S_2 at $t = \delta_1 + \delta_{12}$ leads to refocusing of this initial evolution of S_1 with a probability of 50%. Dipolar evolution of the first spin therefore effectively initiates either at $t = \delta_1$, where the spin gets excited, or at $t = \delta_1 + 2\delta_{12}$, since the initial evolution is refocused. Note that this cosine factor has been analyzed numerically for a nitroxide spectrum at Q-band frequencies[23]. In the context of that study, evolution of the first spin during δ_{12} was considered to account for potential generation of double-quantum coherence.

For the modulated signal, chirp excitation combined with the distribution of resonance offsets Ω_1 and Ω_2 results in a distribution of δ_1 and δ_{12} delays. By assuming uniform excitation pulses, the distribution of δ_1 can be approximated based on the frequency modulation function of the pulse and the shape of the nitroxide spectrum. Using the experimental parameters from the previous section, the δ_1 distribution shown in black in Fig. 2b is obtained. Note that our approach to uniform excitation results in non-linear frequency sweep functions[13], which means that the shape of the δ_1 distribution represents the nitroxide spectrum projected to the non-linear time-frequency relationship of the 128 ns long excitation pulse.

The distribution of δ_{12} is more subtle, since the mutual orien-

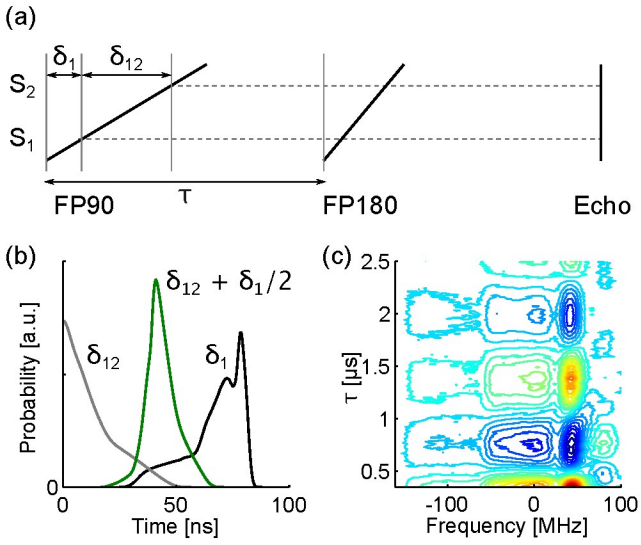

Fig. 2 Dipolar modulation in two-pulse echo decay. (a) 2:1 chirp echo pulse sequence with FP90 excitation pulse and FP180 refocusing pulse represented schematically using the time-frequency profile of a linear frequency sweep. The pulse delay τ as well as the two delays δ_1 and δ_{12} determine the timing of the pulse sequence. Accordingly, the spin S_1 is always excited first at $t = \delta_1$, while spin S_2 is excited upon an additional delay of δ_{12}. (b) Distribution of delays δ_{12} (gray), $\delta_{12} + \delta_1/2$ (green), and δ_1 (black) obtained with the nitroxide spectrum and pulse modulation functions from Section 3.1. (c) FT of two-pulse chirp echo as a function of the inter-pulse delay τ. The color scale from red to blue corresponds to normalized amplitudes from 1.0 to -0.56.

tation between the coupled spins needs to be considered. In particular, excitation of the first spin selects a certain orientation of the excited spin. In presence of orientational correlations, this also constrains the possible orientations of the coupled partner spin. For the present consideration on frequency dispersion, this selection of mutual orientations is neglected. As a consequence, an approximation to δ_{12} can be calculated based on the nitroxide lineshape and the time-frequency profile of the excitation pulse. The resulting distribution of δ_{12} is shown by the gray curve in Fig. 2b. The large probability amplitude at short times originates from spins with small resonance offset, which is most probable in the vicinity of the principal nitroxide peak. Orientational correlations, which we neglected at this point, will modify the shape of the δ_{12} distribution. Nevertheless, the overall spread of δ_{12} times remains bound to $\delta_{12} < 50$ ns, as obtained here.

With the spread in δ_{12} over a time range of up to 50 ns, it is possible to get a boundary for the second cosine factor in Eq. (4). For the first cosine factor, the sum $\delta_{12} + \delta_1/2$ is relevant. The distribution of this sum is shown by the green curve in Fig. 2b. Interestingly, the spread of this distribution is comparable to the spread over 50 ns in the summands. Moreover, the distribution has a rather well defined centered peak with full width at half maximum (FWHM) of 12 ns. The reason for this is the interdependence between δ_1 and δ_{12}. In fact, the sum $\delta_1 + \delta_{12}$ cannot exceed the duration of the first pulse, which holds for any frequency modulation function.

As a result of the $\delta_1 + \delta_{12}$ distribution, 50 ns is an upper limit for the spread of the time argumented in all the cosine factors for the two-pulse chirp echo. This corresponds to an inverse timescale of 20 MHz and must be fast compared to $\omega_{dd}/(2\pi)$. This is clearly the case for spin pairs with distances $r > 3.7$ nm, where dipolar frequencies are below 2 MHz. Given that the first cosine factor has only an FWHM of 12 ns, it may even be possible to obtain significant modulations for distances down to 2.5 nm. However, the asymmetry between the evolution of spin 1 and spin 2 due to the additional cosine factor becomes significant at these shorter distances. In fact, this was confirmed by simulations of the interference effect responsible for the additional term, which were performed using pulsing conditions that are comparable to our experiment[23].

Experimentally, the dipolar modulation of the FT EPR spectrum for our model compound with 4 nm spin-spin distance is shown in Fig. 2c. As one would expect for this spin-spin distance and our pulses, no apparent frequency dispersion in the dipolar modulation pattern is visible for frequency offsets below 50 MHz. However, at frequencies beyond 50 MHz, the modulation pattern is altered considerably. The reason for this are correlated spin-spin orientations, which will be analyzed in more detail in the next section using the SIFTER experiment. Note that the two-pulse chirp echo sequence applied here is not only modulated by dipolar frequencies, but also contains nuclear ESEEM frequencies and a decay due to loss of phase coherence. Even though rather pronounced dipolar modulations are possible with this pulse sequence, these additional contributions complicate the extraction of reliable distances. Moreover, the dipolar modulations may be a complication if chirp ESEEM techniques[31] are applied to systems involving multiple electron spins with dipolar coupling.

3.3 EPR-correlated SIFTER

The SIFTER pulse sequence using non-selective monochromatic pulses is shown on the top row of Fig. 3. The pulses ① and ③ are $\pi/2$ pulses in phase quadrature and realize the solid echo subsequence to refocus the evolution under the dipolar coupling. The pulses ② and ④ are π pulses and refocus the resonance offset. For the two-spin system, as defined in Eq. 1, the echo at $t_{det} = 2(\tau_1 + \tau_2)$ is modulated according to[7]

$$\left\langle \hat{S}_{y,i} \right\rangle (t_{det}) = \cos\left(\omega_{dd}(\tau_1 - \tau_2)\right) \tag{6}$$

where the label i stands for either S_1 or S_2.

In order to implement the SIFTER pulse sequence with chirp pulses for 2D correlation spectroscopy, the sequence is designed to refocus the resonance offset for spin echoes free of frequency-dispersion. This constrains the relative pulse durations of the four pulses and led to the choice of a 2 : 2 : 2 : 1 scheme. The time-frequency profiles of the four pulses are shown in the second row of Fig. 3.

The basic idea behind this scheme is that pulse ③ should not affect the evolution of the resonance offset, as it is the case for SIFTER with monochromatic pulses. This implies that the spin echo produced by pulses ① and ② must have the same frequency dispersion as pulse ③. In the row labeled 'Offset' in Fig. 3, the frequency dispersion of this echo is shown in orange. For a non-dispersed echo at the detection position, the pulse durations of the last two pulses must therefore obey a 2 : 1 relation. For the first two pulses, there are actually various solutions for generating an echo with frequency dispersion over a normalized duration of 2. One could, for instance, also use 4 : 3 : 2 : 1 or 3 : 2.5 : 2 : 1, these schemes do, however, prolong the durations of the first two pulses.

An important experimental aspect of this pulse sequence is that there are two π pulses for refocusing of the resonance offset. In fact, the subsequence realized by pulses ①, ②, and ④ acts on the resonance offset in the same way as a 2 : 2 : 1 refocused primary echo sequence. This 2 : 2 : 1 sequence has been given the acronym *ABSTRUSE* and has been shown to mutually compensate dynamical phase shifts introduced by each of the π pulses[47]. Experimentally, this reduces signal losses originating from spectral and spatial inhomogeneities in the dynamical phase shift, which, in principle, allows for almost perfect refocusing pulses in the adiabatic limit[23].

To analyze the dipolar evolution during this 2:2:2:1 sequence,

it is important to realize that pulse ③ swaps anti-phase coherence from one of the coupled spins to the other[48]. This is schematically represented in the two rows labeled 'Dipolar' in Fig. 3. The upper of these rows corresponds to phase acquisition on S_1 up to pulse ③, which is then transferred to S_2 and detected at the echo position. The lower of these rows illustrates the opposite scenario. When comparing the two pathways, one would expect an asymmetry between S_1 and S_2, similar to the 2:1 echo sequence analyzed in the previous section. For the echo contribution of S_2, application of the product operator formalism according to Section 2.3 results in

$$\langle \hat{S}_{y,2} \rangle (t_{\mathrm{det}}) = \cos(\omega_{\mathrm{dd}}(\tau_1 - \tau_2 + \delta_1/2 - \delta_{12}/2)) \cdot \cos(\omega_{\mathrm{dd}}\delta_{12}/2) \quad (7)$$

where the first cosine factor includes the expected dependence on $\tau_1 - \tau_2$ with corrections due to the chirp excitation. The second cosine factor is identical as in Eq. (4) and is of the same origin. In particular, the modulated contribution of S_2 evolved initially on S_1, where the effect described in the previous section introduces this cosine factor. Knowing the origin of the second cosine factor, one can actually rationalize the argument of the first cosine factor by considering the effect of all pulses on dipolar evolution (see ESI).

The echo contribution by S_1 is more complicated, because the order of swapping anti-phase coherence is reversed at pulse ③, which introduces additional pathways. The full expression is shown in the ESI. Here, we just show the contributions with $\tau_1 - \tau_2$ dependence, which results in

$$\langle \hat{S}_{y,1} \rangle (t_{\mathrm{det}}) = \cos(\omega_{\mathrm{dd}}(\tau_1 - \tau_2 + \delta_1/2 - \delta_{12}/2)) \cdot \left(\frac{3}{4} + \frac{1}{4}\cos(\omega_{\mathrm{dd}}\delta_{12})\right) \quad (8)$$

where the first cosine factor is equivalent to Eq. (7) and the second factor has a dependence on $\omega_{\mathrm{dd}}\delta_{12}$. An analysis of the spread in all evolution pathways is given in the ESI. In brief, the 2:2:2:1 SIFTER sequence has a larger overall spread in phases than the 2:1 chirp echo sequence. Nevertheless, the dipolar frequencies related to our model compound are still in a range where it is reasonable to neglect the contributions from δ_1 and δ_{12}.

This expectation is supported by our experimental observations of pronounced and extended dipolar oscillations. As an example, a 1D SIFTER time trace is depicted in Fig. 4, showing both the real (black) and imaginary (gray) components. This dataset was obtained by integration of echo transients during post-processing, in such a way as to correspond to the dipolar modulation of the principal peak of the nitroxide spectrum. As is readily seen, dipolar modulations extend over several oscillation periods due to the stiffness of the model compound.

It is important to point out that SIFTER entails unwanted dipolar evolution pathways due to imperfections of the inversion pulses[7,29]. These imperfections lead to refocusing of the dipolar evolution at ② or ④ and result in residual modulations with zero-time at the beginning and the end of the SIFTER trace. These modulations depend on either τ_1 or τ_2, in such a way that the oscillation frequency is half the oscillation fre-

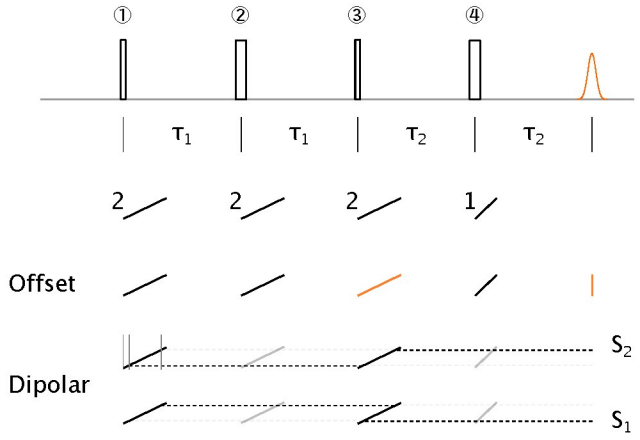

Fig. 3 Four-pulse SIFTER and FT EPR implementation using chirp pulses. First row from top: Pulse sequence for monochromatic pulses, where the length of each pulse is illustrated according to the flip angle of either $\frac{\pi}{2}$ or π. The Gaussian profile at the end denotes the position of the detected echo. Second row: Graphical representation of chirp SIFTER with pulse length ratios 2 : 2 : 2 : 1, as indicated by the numbers next to the time-frequency profiles of the pulses (black). Third row with label 'Offset': Subsequence to refocus the resonance offset based on a 2 : 2 : 1 scheme. The orange line at position ③ denotes the time-frequency profile of the primary echo generated by the first two pulses. Last two rows with label 'Dipolar': Pathways of dipolar phase acquisition that result in the modulation detected on either S_1 (bottom) or S_2 (top).

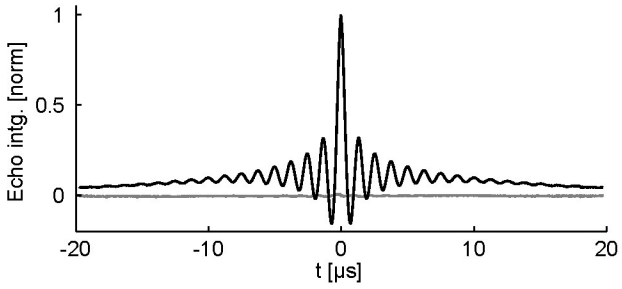

Fig. 4 One-dimensional SIFTER data by integration of the echo transient, showing real (black) and imaginary (gray) component. Here, the echo integral corresponded to the spin packets at the maximum of the nitroxide spectrum. All the timings and pulse parameters for this experiments are described in Section 2.2.

quency of the intended SIFTER oscillation. To separate these residual modulations, we recorded SIFTER data at 12 different echo positions $2(\tau_1+\tau_2)$ (see Section 2.2 for details). In this way, the phase of the SIFTER oscillation remained unchanged, whereas the phase of the residual modulations was varied over a full oscillation period. Accordingly, averaging the 12 datasets effectively canceled those residual modulations, as can be recognized by the absence of such half-frequency modulations in the data shown in Fig. 4 and also in 2D EPR-correlated SIFTER data (see ESI). Moreover, variation of the residual modulations allowed to quantify the modulation depth of these unwanted pathways. In particular, the residual modulation at the beginning of the trace due to imperfections in ④ had a peak-to-peak modulation amplitude of 3.5%. The residual modulation at the end of the trace due to imperfections in ② had a peak-to-peak modulation amplitude of 6%. The larger modulation amplitude due to ② can be related to the smaller nominal tilt angle β_{LZSM} of pulse ② as compared to pulse ④ (157° vs 165°).

Besides the suppression of these weak residual modulations by averaging, there may still be room for reducing the modulation amplitude in the first place. In particular, the pulses ② and ④ did not have maximum pulse amplitude due to the pulse optimization scheme employed here (see Section 2.2). For best artifact suppression, the pulse amplitudes should be maximized for best inversion performance. However, it must be noted that the two π pulses realize the aforementioned ABSTRUSE scheme, such that it is possible to mutually compensate the transient Bloch-Siegert phase shifts exerted by each of the two frequency-swept refocusing pulses. In general, such a compensation is advisable, since transient phase shifts potentially cause signal loss arising from spatial inhomogeneity of the driving field ν_1. As we have shown recently[23], the dynamical phase shift exerted by a frequency-swept refocusing pulse is proportional to the adiabaticity factor Q_{crit}. To avoid signal losses due to non-compensated transient phase shifts while maximizing suppression of the residual modulations, one should therefore only use the maximum available field strength for pulse ④, while keeping pulse ② at a field strength reduced by $\sqrt{2}$. At maximum field amplitude for pulse ④, our spectrometer can actually realize $\beta_{\mathrm{LZSM}} = 173°$ for the 64 ns pulse.

For 2D EPR-correlated SIFTER data, the echo transients were processed by two-dimensional Fourier-transform. Upon the first FT along the EPR dimension, a Gaussian background decay has been fitted to EPR-correlated SIFTER traces. Due to an artificial contribution of quartz in the EPR spectrum (see below), subtraction of this Gausssian background decay yielded the best results. Before computing the second FT along the SIFTER dimension, the remaining constant offset was subtracted. Due to the long dipolar evolution window, it was also possible to use a Chebychev window to apodize EPR-correlated SIFTER traces for improving spectral quality (see ESI). With a shorter dipolar evolution window, such an apodization may no longer be admissible.

The magnitude of the 2D correlation spectrum obtained according to the above description is shown in Fig. 5a. The FT EPR spectrum on the right hand side corresponds to the real part of the FT at $t = 0$ and approves refocusing of the resonance offset. However, around an EPR offset of -80 MHz, an unusual peak in the FT EPR spectrum is observed (see arrow). This peak is related to E' centers in quartz of the sample tube, which we often see at concentrations below 100 μM. This quartz artifact caused the peak around zero dipolar frequency observed at the corresponding position in the 2D correlation pattern and also influenced the amplitude of the main dipolar ridge around ± 0.8 MHz. In addition to this artifact caused by quartz, background correction resulted in a discontinuity in dipolar spectra around the zero frequency.

Other than these artifacts, the 2D correlation spectrum encodes the frequency splitting between dipolar doublets throughout the entire EPR spectrum. The SIFTER projection above the correlation spectrum resembles a Pake pattern. The dependence of the dipolar coupling on EPR frequency is due to orientational effects, as illustrated in the following. In particular, normalized SIFTER data at three distinct EPR frequencies labeled *i*, *ii* and *iii* are illustrated in Figs. 5b and c in time domain and in frequency domain, respectively. The positions within the EPR spectrum are indicated by the horizontal markers in the correlation spectrum in panel (a). Positions *i* and *iii* correspond to canonical orientations along the *x* and *z* axis in the nitroxide PAS, respectively. At position *ii* a multitude of spin orientations contribute to the EPR spectrum.

In order to relate the orientations of the nitroxide to the spin-spin orientations, the structure of the nitroxide-ruler is shown in Fig. 5d. The two vectors labeled *i* and *iii* denote the orientations of the static magnetic field with respect to the ruler. Because the N-O bond is collinear with the inter-spin vector, the canonical orientation along *x* in the nitroxide PAS corresponds to a parallel alignment between the magnetic field and the inter-spin vector. The dipolar interaction for such a configuration results in a splitting by twice the fundamental splitting ω_{dd}, which corresponds to the parallel singularity at the shoulders of the Pake pattern. The canonical orientation along *z* in the nitroxide PAS corresponds to a orthogonal alignment between the magnetic field and the inter-spin vector. In this configuration, the dipolar interaction results in a splitting by the fundamental frequency ω_{dd}, which corresponds to the transverse singularity at the horns of the Pake pattern. Note that due to free rotation about the triple bonds, direction *iii* is not necessarily perpendicular with respect to the paper plane, as the structure in Fig. 5d would suggest. Nevertheless, direction *iii* is always perpendicular with respect to the spin-spin vector, as long as the residual flexibility of the linker[43] is neglected.

The Pake singularities predicted from the structure of the ruler are reproduced in the SIFTER slices in panels (b) and (c). In fact, the double frequency at the parallel singularity at position *i* and the fundamental frequency at the transverse singularity at position *iii* are readily identified. At position *ii*, the contribution of several orientations results in a dipolar spectrum resembling a Pake pattern with somewhat attenuated shoulders.

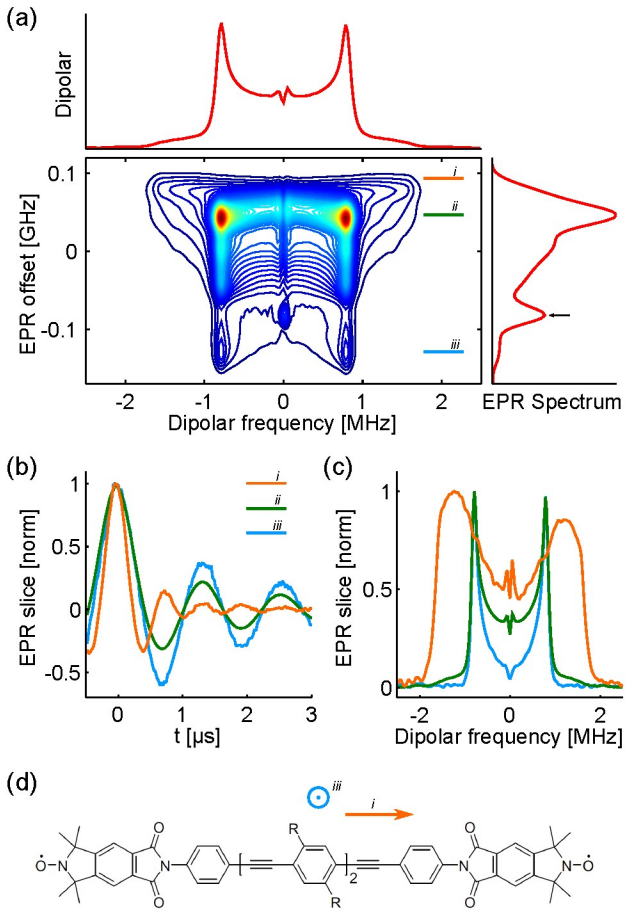

Fig. 5 2D EPR-correlated SIFTER. (a) Magnitude 2D FT of SIFTER echoes with background correction as described in the text. The dipolar spectrum above the correlation spectrum is the projection of the illustrated 2D spectrum. The EPR spectrum on the right is the real part of the FT for $t = 0$. The arrow denotes an artifact due to E' centers in quartz of the sample tube. Relevant EPR positions are indicated by the horizontal markers labeled *i*, *ii* and *iii*. (b, c) Normalized SIFTER traces at relevant EPR positions in time domain (b) and in frequency domain (c). (d) Structure of the investigated nitroxide-ruler (see also[42,43]). The vectors in blue and orange indicate the orientations of the magnetic field at the EPR positions *i* and *iii*. Note that there is no way to differentiate between positive and negative direction in the high-temperature approximation.

The pronounced asymmetry in the dipolar spectrum observed at postion *i* is probably due to the steep ascent in the EPR lineshape. In fact, pronounced asymmetries have also been observed at the fundamental dipolar frequency in regions of steep ascent around the main peak of the EPR spectrum (data not shown).

Based on these considerations, we therefore conclude that it is, in principle, possible to use the 2D SIFTER technique to study the relative orientation between nitroxide spin labels. At present, such studies are performed predominantly using the four-pulse DEER experiment at W-band frequencies recorded for a set of pump and observation positions[49–52]. Multiple DEER experiments are therefore required, which results in a longer acquisition time than for 2D SIFTER.

However, it is important to point out the differences between DEER and 2D SIFTER with respect to orientation selection. In DEER, the observation frequency selects the relevant position in the EPR spectrum. In the 2D SIFTER correlation spectrum, this corresponds to the EPR frequency offset. In presence of orientation selection, however, the dipolar pattern obtained with DEER and 2D SIFTER may be entirely different. The reason is that the pump position in DEER selects the orientation of the coupled spin partner, whereas 2D SIFTER reveals the dipolar spectrum due to all coupled spin partners. With pump and observation positions at canonical orientations in the nitroxide PAS, DEER therefore probes specific geometrical correlations between the orientations of the coupled spins. 2D SIFTER on the contrary reveals geometrical correlations between the orientation of one spin and the inter-spin vector, without information on the orientation of the coupled spin (see below: pseudo-secular contributions in principle encode this information). Accordingly, there are four angles that determine the correlation pattern in 2D SIFTER data, namely the two angles required to describe the orientation of the inter-spin vector related to each of the two spins. On the contrary, DEER data with orientation selection encodes five angles[53], so that the fewer parameters in 2D SIFTER may simplify the extraction of orientational information from experimental data.

Since the orientation between the inter-spin vector and the spin-label are identical for both spin labels of the nitroxide-ruler investigated here, both spin labels contribute in the same way to the 2D correlation spectrum. In a simulation study of six-pulse DQC with monochromatic pulses[37], 2D correlation spectra of spin pairs with different relative orientation to the inter-spin vector have been calculated. For these cases, the 2D correlation spectrum is a superposition of two spectra (see for instance Fig. 8c in ref [37]). Note that to date, 2D correlation spectra by six-pulse DQC with monochromatic pulses have been demonstrated at 17.25 GHz microwave frequency by combining two datasets covering one half of the EPR spectrum each[4].

An additional relevant difference between DEER and 2D SIFTER is the influence of pseudo-secular contributions of the dipolar interaction on experimental data. Such contributions originate from spin pairs, where the frequency separation is comparable to the dipolar interaction, so that the weak coupling approximation is no longer appropriate[8]. While spin pairs that are not in weak coupling conditions can be suppressed by the choice of the frequency separation between pump and observer spins in DEER, this is not possible in SIFTER[7]. As suggested previously[37], the pseudo-secular contribution in 2D correlation spectra provides additional information on the frequency separation between coupled spin pairs. Provided that these contributions can be resolved experimentally, information on the orientation of the coupled spin partner could in principle be extracted from 2D SIFTER spectra. However, an analysis of chirp effects related to pseudo-secular contributions is out of the scope of the present work. In particular, such contributions are most prominent at short distances[7], where our present analysis predicts considerable perturbation of the dipolar evolution under the secular coupling due to chirp effects.

In fact, the chirp effects are an important restriction of the technique presented here. Spectrometers with reduced power and bandwidth require longer pulses, which further constrain the applicable distance range. In particular at frequencies above Q band, where the principal components of the nitroxide *g*-tensor become better resolved, EPR-correlated PDS with chirp pulses may require advanced high-power instrumentation[54,55]. Clearly, a pulse sequence which refocuses both the resonance offset and the dipolar coupling would significantly alleviate this limitation. In this respect, previous considerations on NMR with scalar coupling using chirp pulses[41] may gain relevance in EPR.

4 Summary

Highly uniform excitation with bandwidths beyond 100 MHz became feasible at Q band using bandwidth-compensated chirp pulses with a 200 W power amplifier. These pulses enable 2D correlation spectroscopy capabilities at Q band for nitroxides in disordered solids. In particular, we have shown for the first time that the dipolar spectrum can be correlated to the entire nitroxide spectrum. Importantly, these EPR-correlated dipolar spectra do not only contain information on inter-spin distances, but also on the orientation of the spin-spin vector with respect to the molecular frames of the two nitroxide labels[37]. For our investigated model compound, the experimental correlation pattern corroborates the expectation based on the structure of the compound.

Thanks to the multiplex advantage of such 2D correlation experiments, orientation information can be accessed in one single experiment, whereas the established 1D techniques require a combination of multiple experiments. Information on geometrical correlation within spin-labeled biomacromolecules can therefore be obtained at a reduced experimental overhead. Even if the problem of extracting the geometrical coordinates from experimental data is likely to remain a very difficult problem also with these techniques, the dispersion of Pake singularities within the correlation pattern may provide quick information on conformational flexibility.

An important limitation of the technique is potential interference in the dipolar evolution due to frequency-swept excitation. In fact, multiple dipolar evolution pathways have been identified based on pulse sequence calculations. Since these pathways acquire slightly different phases, interference between these pathways must be avoided. With the performance of our AWG spectrometer, the pulse requires only 50 ns to sweep its frequency through the entire nitroxide spectrum. As a result, our approach is expected to provide reliable data down to distances of 3.4 nm or even slightly below.

5 Acknowledgements

René Tschaggelar is acknowledged for design of the loop-gap resonator. Oliver Oberhänsli is acknowledged for the construction of the resonator and mechanics support for the Q-band extension. We thank Muhammad Sajid and Adelheid Godt for the synthesis of the rigid model compound and Takuya Segawa as well as Yevhen Polyhach for fruitful discussions. This work was supported by the Swiss National Science Foundation (Grant No. 20020_157034).

References

1 G. Jeschke and Y. Polyhach, *Phys. Chem. Chem. Phys.*, 2007, **9**, 1895–1910.
2 O. Schiemann and T. F. Prisner, *Q. Rev. Biophys.*, 2007, **40**, 1–53.
3 G. Jeschke, *Annu. Rev. Phys. Chem.*, 2012, **63**, 419–446.
4 P. P. Borbat and J. H. Freed, in *Structure and Bonding*, ed. C. R. Timmel and J. R. Harmer, Springer Berlin Heidelberg, 2013, vol. 152, pp. 1–82.
5 M. Pannier, S. Veit, A. Godt, G. Jeschke and H. Spiess, *J. Magn. Reson.*, 2000, **142**, 331 – 340.
6 P. P. Borbat and J. H. Freed, *Chem. Phys. Lett.*, 1999, **313**, 145 – 154.
7 G. Jeschke, M. Pannier, A. Godt and H. Spiess, *Chem. Phys. Lett.*, 2000, **331**, 243 – 252.
8 A. Schweiger and G. Jeschke, *Principles of Pulse Electron Paramagnetic Resonance*, Oxford University Press, USA, 2001.
9 V. Yudanov, K. Salikhov, G. Zhidormirov and Y. Tsvetkov, *Theor. Exp. Chem.*, 1972, **5**, 451–455.
10 J. Powles and P. Mansfield, *Phys. Lett.*, 1962, **2**, 58 – 59.
11 K. Salikhov and I. Khairuzhdinov, *Appl. Magn. Reson.*, 2015, **46**, 67–83.
12 P. E. Spindler, Y. Zhang, B. Endeward, N. Gershernzon, T. E. Skinner, S. J. Glaser and T. F. Prisner, *J. Magn. Reson.*, 2012, **218**, 49 – 58.
13 A. Doll, S. Pribitzer, R. Tschaggelar and G. Jeschke, *J. Magn. Reson.*, 2013, **230**, 27 – 39.
14 P. E. Spindler, S. J. Glaser, T. E. Skinner and T. F. Prisner, *Angew. Chem. Int. Ed.*, 2013, **52**, 3425–3429.

15 M. Tseitlin, G. A. Rinard, R. W. Quine, S. S. Eaton and G. R. Eaton, *J. Magn. Reson.*, 2011, **211**, 156 – 161.

16 N. Devasahayam, R. Murugesan, K. Matsumoto, J. Mitchell, J. Cook, S. Subramanian and M. Krishna, *J. Magn. Reson.*, 2004, **168**, 110 – 117.

17 J. S. Hodges, J. C. Yang, C. Ramanathan and D. G. Cory, *Phys. Rev. A*, 2008, **78**, 010303.

18 G. D. Fuchs, V. V. Dobrovitski, D. M. Toyli, F. J. Heremans and D. D. Awschalom, *Science*, 2009, **326**, 1520–1522.

19 R. H. Crepeau, A. Dulic, J. Gorcester, T. R. Saarinen and J. H. Freed, *J. Magn. Reson.*, 1989, **84**, 184 – 190.

20 M. Garwood and L. DelaBarre, *J. Magn. Reson.*, 2001, **153**, 155 – 177.

21 F. D. Giacomo and E. E. Nikitin, *Phys. Uspekhi*, 2005, 515.

22 J. W. Zwanziger, S. P. Rucker and G. C. Chingas, *Phys. Rev. A*, 1991, **43**, 3232–3240.

23 G. Jeschke, S. Pribitzer and A. Doll, *J. Phys. Chem. B*, 2015, **119**, 13570–13582.

24 J. Baum, R. Tycko and A. Pines, *Phys. Rev. A*, 1985, **32**, 3435–3447.

25 A. Doll, M. Qi, N. Wili, S. Pribitzer, A. Godt and G. Jeschke, *J. Magn. Reson.*, 2015, **259**, 153 – 162.

26 A. Doll, M. Qi, S. Pribitzer, N. Wili, M. Yulikov, A. Godt and G. Jeschke, *Phys. Chem. Chem. Phys.*, 2015, **17**, 7334–7344.

27 P. E. Spindler, I. Waclawska, B. Endeward, J. Plackmeyer, C. Ziegler and T. F. Prisner, *J. Phys. Chem. Lett.*, 2015, **6**, 4331–4335.

28 P. P. Borbat, E. R. Georgieva and J. H. Freed, *J. Phys. Chem. Lett.*, 2013, **4**, 170–175.

29 P. Schöps, P. E. Spindler, A. Marko and T. F. Prisner, *J. Magn. Reson.*, 2015, **250**, 55 – 62.

30 A. Doll and G. Jeschke, *J. Magn. Reson.*, 2014, **246**, 18 – 26.

31 T. F. Segawa, A. Doll, S. Pribitzer and G. Jeschke, *J. Chem. Phys.*, 2015, **143**, 044201.

32 J. A. Ferretti and R. R. Ernst, *J. Chem. Phys.*, 1976, **65**, 4283–4293.

33 J. M. Böhlen and G. Bodenhausen, *J. Magn. Reson.*, 1993, **102**, 293 – 301.

34 D. Kunz, *Magn. Reson. Med.*, 1987, **4**, 129–136.

35 J. M. Böhlen, M. Rey and G. Bodenhausen, *J. Magn. Reson.*, 1989, **84**, 191 – 197.

36 S. Lee, B. R. Patyal and J. H. Freed, *J. Chem. Phys.*, 1993, **98**, 3665–3689.

37 S. Misra, P. Borbat and J. Freed, *Appl. Magn. Reson.*, 2009, **36**, 237–258.

38 P. P. Borbat and J. H. Freed, in *Distance Measurements in Biological Systems by EPR*, ed. L. J. Berliner, G. R. Eaton and S. S. Eaton, 2002, vol. 19, pp. 383–459.

39 O. Sørensen, G. Eich, M. H. Levitt, G. Bodenhausen and R. Ernst, *Prog. Nucl. Magn. Reson. Spectrosc.*, 1984, **16**, 163–192.

40 S. Boentgens, *Personal communication*.

41 I. Burghardt, J.-M. Böhlen and G. Bodenhausen, *J. Chem. Phys.*, 1990, **93**, 7687–7697.

42 M. Sajid, G. Jeschke, M. Wiebcke and A. Godt, *Chem. Eur. J.*, 2009, **15**, 12960–12962.

43 G. Jeschke, M. Sajid, M. Schulte, N. Ramezanian, A. Volkov, H. Zimmermann and A. Godt, *J. Am. Chem. Soc.*, 2010, **132**, 10107–10117.

44 J. R. Klauder and P. W. Anderson, *Phys. Rev.*, 1962, **125**, 912–932.

45 A. M. Raitsimring, K. M. Salikhov, B. A. Umanskii and Y. D. Tsvetkov, *Sov. Phys Solid State*, 1974, **16**, 492.

46 V. Yudanov, K. Salikhov, G. Zhidomirov and Y. D. Tsvetkov, *J. Strukt. Khim*, 1969, **10**, 732–734.

47 K. E. Cano, M. A. Smith and A. Shaka, *J. Magn. Reson.*, 2002, **155**, 131 – 139.

48 R. Ernst, G. Bodenhausen and A. Wokaun, *Principles of Nuclear Magnetic Resonance in One and Two Dimensions*, Clarendon Press, 1990.

49 Y. Polyhach, A. Godt, C. Bauer and G. Jeschke, *J. Magn. Reson.*, 2007, **185**, 118 – 129.

50 A. Savitsky, A. A. Dubinskii, H. Zimmermann, W. Lubitz and K. Möbius, *J. Phys. Chem. B*, 2011, **115**, 11950–11963.

51 I. Tkach, S. Pornsuwan, C. Hobartner, F. Wachowius, S. T. Sigurdsson, T. Y. Baranova, U. Diederichsen, G. Sicoli and M. Bennati, *Phys. Chem. Chem. Phys.*, 2013, **15**, 3433–3437.

52 M. A. Stevens, J. E. McKay, J. L. S. Robinson, H. EL Mkami, G. M. Smith and D. G. Norman, *Phys. Chem. Chem. Phys.*, 2016, **18**, 5799–5806.

53 R. G. Larsen and D. J. Singel, *J. Chem. Phys.*, 1993, **98**, 5134–5146.

54 W. Hofbauer, K. A. Earle, C. R. Dunnam, J. K. Moscicki and J. H. Freed, *Rev. Sci. Instrum.*, 2004, **75**, 1194–1208.

55 P. A. S. Cruickshank, D. R. Bolton, D. A. Robertson, R. I. Hunter, R. J. Wylde and G. M. Smith, *Rev. Sci. Instrum.*, 2009, **80**, 103102.